Atmospheric Environment Vol. 25A, No. 5/6, pp. 1039–1053, 1991.
Printed in Great Britain.

0004–6981/91 $3.00 + 0.00

AN INVESTIGATION OF AEROSOL MICROSTRUCTURE ON VISUAL AIR QUALITY

SI-CHEE TSAY, GRAEME L. STEPHENS and THOMAS J. GREENWALD
Department of Atmospheric Science, Colorado State University, Fort Collins, CO 80523, U.S.A.

(*First received* 10 *October* 1988 *and in final form* 2 *August* 1990)

Abstract—Visibility modeling requires a proper description of the optical properties of atmospheric pollutants and an accurate simulation of the physical processes of light propagation in the atmosphere. The objectives of this paper are to study the effects of various microstructures of atmospheric particles on their optical properties (such as extinction coefficient, probability of scattering, and scattering phase matrix) and consequential influence on the computation of path radiance and contrast.

Mie computations are performed, in which the physical characteristics (e.g. size distribution, solubility, and mixture) of particles and the atmospheric conditions (e.g. moisture) are allowed to vary. A plane–parallel multiple scattering radiation model, utilizing the methods of doubling and adding, is then used to assess the impact of atmospheric pollutants on visibility and visual air quality. The results of this study demonstrate the dependence of sky radiance not only on the aerosol extinction coefficient but on the phase matrix and environmental conditions as well. These results are presented in sky color maps which are created using truecolor imagery.

Key word index: Aerosol microphysics, visibility, contrast, sky color.

1. INTRODUCTION

Atmospheric aerosols affect not only visibility but also daily weather, the climate of the Earth, and it has been speculated in some instances even the survival of species on Earth. One of the most apparent influences of these aerosols is on the transfer of visible light in the terrestrial atmosphere which is especially important to problems of visibility and the perceived visual air quality.

Visibility modeling requires a proper description of the optical properties of these atmospheric aerosols and an accurate simulation of the physical processes of light propagation in the atmosphere. Specification of the aerosol optical properties is in fact a complex problem. Many of the past investigations on this subject have focused on the relation of the extinction coefficients to the chemical specification of aerosol mass through empirical/statistical models of multivariate linear regression (e.g. Barone *et al.*, 1978; Ouimette and Flagan, 1982) while other investigators have relied on more physical aerosol models (Sloane, 1984, 1986 among others). Most of these studies have been constrained within the realm of Beer's Law, in which the multiple scattering of light is neglected.

Visibility degradation is a combination of two effects: the attenuation of image forming radiance and the generation of path radiance by the atmospheric molecular and aerosol extinction, including multiple scattering. The difference in the path radiance between scattering dominated and absorption dominated aerosols could be as large as one to two order of magnitude. Consequently, considerations of visibility reduction only on the attenuation of light along the viewing path may produce serious error (e.g. Dave, 1981). Furthermore, the perceived visual air quality is often determined by the color contrast and the loading of aerosols of different microstructure can change the sky color dramatically from clean and blue to turbid and yellowish or to brownish (e.g. Megaw, 1977; Dave, 1980; Groblicki *et al.*, 1981) in a complex manner.

To account for the enhancement of path radiance by aerosol loading and multiple scattering, one needs suitable and accurate methods for computing aerosol optical properties and for simulating atmospheric radiance fields. In section 2 we describe the construction and consideration of atmospheric aerosol models used. Then based on their microstructures, the aerosol optical properties are determined in section 3. In section 4 we first describe a radiative transfer model used to compute intensity fields, contrast and colorimetric parameters for aerosols in a horizontally homogeneous atmosphere. The effects of scattering by air molecules and by a reflecting surface are also included in the model. We then proceed in section 5 to show, from a theoretical perspective, how different microstructure of atmospheric aerosol affects visual air quality; in particular, how it alters the sky intensity field, the contrast of an object viewed along a horizontal path and the perceived color contrast. Truecolor images are used to illustrate the effect of aerosol on sky color. A summary of this study is given in section 6.

2. ATMOSPHERIC AEROSOL MODELS

2.1. *Size distribution*

In practice, a volume of aerosols is a collection of discrete sized particles with a number concentration

(η, particles per unit volume per radius) that varies with aerosol size. These grouped data are commonly presented in the form of a histogram. However, we may conveniently characterize such a polydispersion in terms of some type of analytical function.

The lognormal distributions are frequently used in describing aerosol size and/or volume distributions (e.g. Davies, 1974), due to their unique properties [cf. Aitchison and Brown (1957) for detailed discussion]. The lognormal size distribution has the form

$$\eta(r)=\frac{N_o}{r\sqrt{2\pi}\ln\sigma_g}\exp\left[-\frac{1}{2}\left(\frac{\ln r/r_m}{\ln\sigma_g}\right)^2\right], \quad (1)$$

where N_o is the total (volume) concentration of aerosols, r_m is the median (or geometric mean) radius and σ_g is the geometric standard deviation. By performing a fundamental transformation and algebraic manipulation, the p-moment of radius (r^p) with respect to the size distribution is readily obtained

$$\int_0^\infty r^p\eta(r)\mathrm{d}r=N_o r_m^p f(p), \quad (2)$$

where $f(p)=\exp\left(\frac{p\ln\sigma_g}{\sqrt{2}}\right)^2$. For example, the effective radius (r_{eff}), which is the ratio of third to second moments of the size distribution (Hansen and Travis, 1974), is an important parameter in characterizing single scattering properties, and is determined by

$$r_{eff}=r_m\exp\left[\frac{5}{2}(\ln\sigma_g)^2\right]. \quad (3)$$

Moreover, when a particle number density is required (such as Mie computation), a known median radius of higher p-moment distribution ($r_{m,p}$; e.g. $p=3$ for volume distribution) can be transferred into number density distribution by utilizing the following transformation

$$r_m=r_{m,p}\exp[-p(\ln\sigma_g)^2]. \quad (4)$$

2.2. *Aerosol mixture*

Microscopic analysis reveals that atmospheric aerosols agglomerate in complex ways. As we will demonstrate, different combinations of aerosol species produce changes of the effective optical characteristics of the aerosols which in turn influence the atmospheric visibility in important ways. In general, there are three types of mixture that can be readily approximated by physical models: external, internal, and volume mixture (e.g. Ackerman and Toon, 1981). Figure 1 shows these three types of aerosol mixtures. The properties of the individual chemical species that comprise the mixture are summed up to represent the effective properties of an external mixing, in which aerosols are mixed as distinct particles without interaction. External mixing is the most frequent assumption used in the literature. The internal mixing is defined such that aerosols exist as a core and/or a shell to form a coated particle. If the aerosol species are combined in fixed proportions, it is referred to as a volume mixture. Bohren (1986), however, argued the applicability and validity of the volume mixture (e.g. the concepts of effective-medium). In this study, we consider a volume mixture only if the aerosols can be mixed homogeneously. For example, the effective indices of refraction are taken to be a combination by volume of the original dry soluble compound and the solution (e.g. water and/or sulphuric acid) when they are mixed. For the case of insoluble compounds, then the particle is considered to be an as internal mixture with a coating structure.

2.3. *Chemical species and solubility*

Aerosols sampled in the real world are generally not single-sized or single-moded, instead they often have sizes in the ranges referred to as the nuclei mode, the accumulation mode and the coarse mode. In most cases the different modes are associated with varying aerosol species (Friedlander, 1970; Nilsson, 1979; Blanchet and List, 1983). For example, most of the sea salt aerosols are in the coarse mode. The size distribution of Los Angeles smog was well fitted by Davies (1974) using up to seven lognormal distributions, while Egan (1982) used generalized gamma distributions to simulate and examine a variety of aerosol measurements. Therefore, a wide range composition of aerosol species can be modeled by changing the parameters of these analytic functions, and the optical

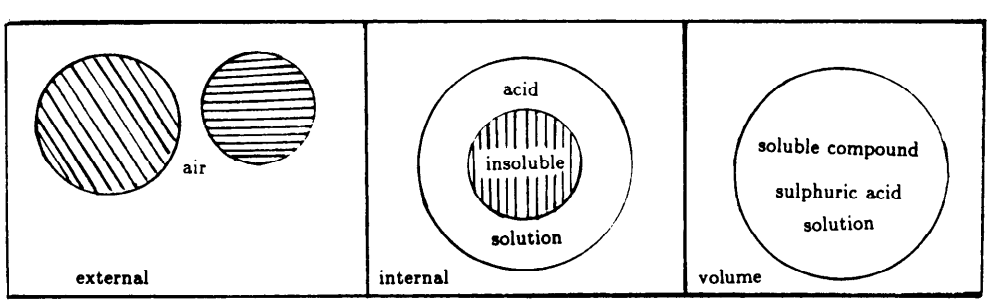

Fig. 1. Schematic representation of aerosol mixtures: (a) external mixing, (b) internal mixing with coating structure and (c) homogeneous mixing within a volume.

properties can also be examined extensively in terms of these distributions.

In a moist environment under supersaturation, water vapor is first absorbed by the soluble aerosols. Consequently, the water activity also changes the aerosol size distribution and the effective indices of refraction. To consider these changes, an iterative scheme developed by Shettle and Fenn (1979) and extended for coated spheres by Blanchet and List (1983) is adopted here to infer the wetted aerosol sizes and effective indices of refraction. The observed relation between water uptake and water activity for various types of aerosols and sulphuric acid (Hänel, 1976; Nair and Vohra, 1975) is used in the model.

3. AEROSOL OPTICAL PROPERTIES

3.1. *Single particle*

The optical properties of atmospheric aerosols are closely related to their microstructure and for the purpose of estimating these properties, the assumption that these particles are spheres is invoked. Interaction of radiation with a scattering/absorbing homogeneous sphere is described by Mie theory and is adequately discussed in a number of classic textbooks (e.g. van de Hulst, 1957; Deirmendjian, 1969) and a number of recent, improved Mie scattering algorithms have become available (Wiscombe, 1980, 1989). The physical parameters involved in Mie calculations are the complex refractive index of the sphere relative to the surrounding medium ($m = n_{\text{real}} - in_{\text{imaginary}}$) and the size parameter ($x = \pi d/\lambda$; d for diameter and λ for wavelength). Indices of refraction for different types of aerosols used in this study are adopted from the compilation of Shettle and Fenn (1979). The complete single scattering parameters of extinction (Q_{ext}) and scattering (Q_{sca}) efficiency factors as well as the scattering phase matrix (P_ϑ, the angular distribution and polarization of the scattered radiation related to scattering angle ϑ) are then obtained (cf. Wiscombe, 1980 and 1989 for detailed derivations).

While we assume spherical geometry, the aerosol particles that appear in the atmosphere are generally not spherical in shape. Although liquid aerosols or liquid-coated aerosols (e.g. coating of sulfuric acid solution; Bigg, 1980) are approximately spherical, dry particles tend to be irregular in shape. Pollack and Cuzzi (1980) suggested that for nonspherical particles with $x < \sim 5$ the error may be quite small, due to the light wave only sensing the particle without detailing its shape or variation in composition. Also, studies by Chýlek *et al.* (1976) and Holland and Gagne (1970) indicated that for particles of equal overall dimensions but different shapes, the spherical particle extinction has the highest values. Therefore, Mie computations involving the assumption of sphericity are still appropriate to most cases if proper precautions are made. To account for the structure of concentrical-coated sphere, the more general Aden and Kerker solution (Kerker, 1969) is used in place of the Mie solution. Furthermore, the study of Toon and Ackerman (1981) reconstructed the algorithms to circumvent the numerical instabilities involved in the Aden and Kerker solution of a_n and b_n.

3.2. *Polydispersed particles*

A volume of aerosols typically contains a mixture of particles of different sizes and species. The single scattering parameters (extinction coefficient β_{ext}, probability of scattering $\tilde{\omega}$, and scattering phase matrix P_ϑ), which are ultimately used in multiple scattering radiation models and thus properties that influence the path radiance significantly, can be computed for each individual aerosol species (i) and the associated size distributions

$$\beta^i_{\text{sca}} = \frac{\pi}{k^3}\int_0^\infty x^2 Q_{\text{sca}}(x)\eta(x)\mathrm{d}x$$

$$\beta^i_{\text{ext}} = \frac{\pi}{k^3}\int_0^\infty x^2 Q_{\text{ext}}(x)\eta(x)\mathrm{d}x$$

$$P^i(\vartheta) = \frac{\pi}{k^3\beta^i_{\text{sca}}}\int_0^\infty x^2 Q_{\text{sca}}(x)P(x,\vartheta)\eta(x)\mathrm{d}x, \quad (5)$$

where $k = 2\pi/\lambda$ and $\tilde{\omega}^i = \beta^i_{\text{sca}}/\beta^i_{\text{ext}}$. The final optical properties of the combination of all aerosol species are then weighted properly according to their partition in total volume (Blanchet and List, 1983).

Figure 2 shows, for example, an aerosol size distribution commonly observed in the atmosphere (e.g. Bigg, 1980) and its corresponding characteristic parameters of lognormal functions are listed in Table 1. If each mode of the size distribution is associated with one pure substance, which is assigned as soot, dust-like and sea-salt aerosols, the bulk optical properties

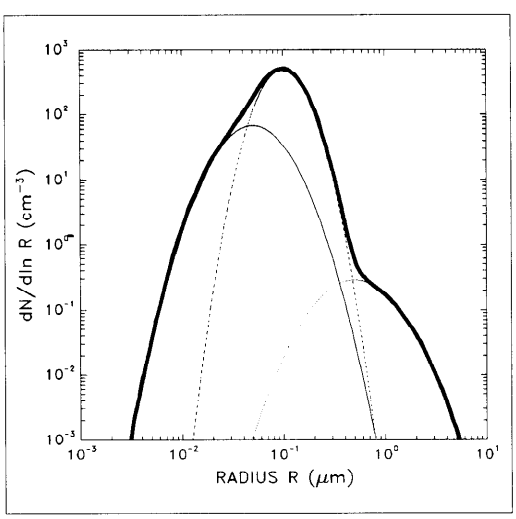

Fig. 2. An aerosol model size distribution which is composed of three lognormal functions and their characteristic parameters are listed in Table 1.

at 0.55 μm wavelength can be obtained according to Equation (5) and are listed in Table 2. The asymmetry factor (g), which is the first moment of the scattering phase function, is computed from Mie theory. The corresponding physical properties of these aerosols are also listed in Table 2. Figure 3 shows the scattering phase functions of individual components and total aerosol mixture. Soot and dust-like aerosols are generally smooth in all scattering angles, with a minimum at about 130°. Since the sea-salt aerosol is relatively large and close to pure scattering, two extreme scattering features are displayed at the forward and backward directions. When all aerosols are mixed externally, the scattering characteristics is thus a composition of each component. The wavelength dependence of the scattering phase matrix is shown in Fig. 4 for three primary colors of red (0.63 μm), green (0.55 μm) and blue (0.45 μm). The major difference of these three phase functions is the increase in backward scattering as wavelength increases, which is caused mainly by the decrease of optical sizes.

To explore the effect of relative humidity on aerosol optical properties, a dry aerosol model is defined and listed in Table 3a. The classification of chemical compound and the index of refraction are adopted from Shettle and Fenn (1979), except for the pure sulphuric acid case which is taken from Nair and Vohra (1975). In the moist environment, the water activity of each aerosol component follows the measurements of Hänel (1976), defined as urban, maritime and continental types. Soot and dust-like particles are not soluble, but with the coating of sulphuric acid they grow through the absorption of water vapor by sulphuric acid. The computed bulk optical properties for three relative humidities are listed in Table 3b. A nonlinear relation between the bulk optical properties and relative humidity is observed. Figure 5 shows the scattering phase functions for relative humidity at 0%, 50% and 90%. The most pronounced changes in the scattering pattern are the dramatic increase in the

Table 1. Size distribution parameters for an aerosol model having lognormal functions. r_m stands for the median radius (μm), σ_g for geometric standard deviation and N_o for total aerosol concentration (cm^{-3})

Mode	r_m	σ_g	N_o
1	0.05	1.8	100
2	0.10	1.5	500
3	0.50	2.0	0.5

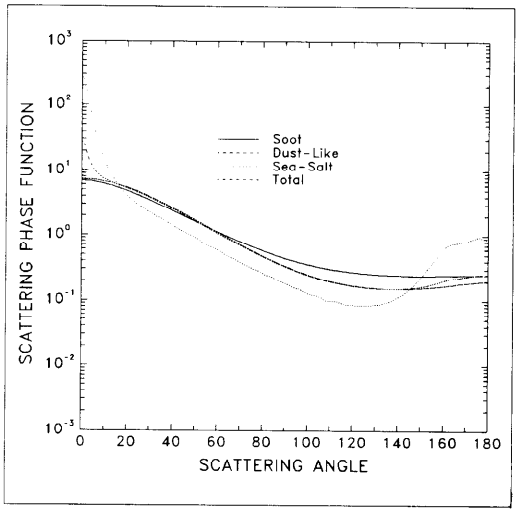

Fig. 3. Scattering phase functions at 0.55 μm wavelength for three pure aerosol substances of (a) —— soot, (b) – – – dust-like, (c) · · · sea-salt, and (d) –·–·– for all components.

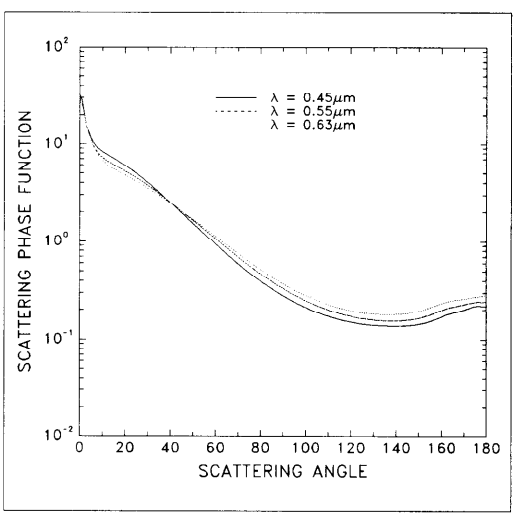

Fig. 4. Wavelength dependence of scattering phase functions of all components, defined as in Fig. 3, for (a) —— 0.45 μm, (b) – – – 0.55 μm, and (c) · · · 0.63 μm.

Table 2. Physical and optical properties for an aerosol model having the size distribution shown in Fig. 2. V_o denotes the total volume of aerosol (μm^3 cm^{-3}); m, the index of refraction at 0.55 μm wavelength; β_{ext}, the extinction coefficient (Km^{-1}); $\tilde{\omega}$, the single scattering albedo; and g, the asymmetry factor

	Physical properties				Optical properties		
	Mode	N_o	V_o	m	β_{ext}	$\tilde{\omega}$	g
Soot	1	100	0.248	1.75–0.440i	0.002781	0.39803	0.5442
Dust-like	2	500	4.388	1.53–0.008i	0.030482	0.95865	0.6213
Sea-salt	3	0.5	2.246	1.50–0.000i	0.002471	1.00000	0.7245
Total	—	600.5	6.882	—	0.035734	0.91787	0.6265

Table 3. As in Table 2, except for different aerosl compositions (%), wavelengths (λ, in μm), and relative humidities (r.h. in %). Notations are the same as in Table 2, except V_w for the total volume of wetted aerosol ($\mu m^3\,cm^{-3}$) and r_{eff} for the effective radius (μm)

(a)

	Soluble	Dust-like	Soot	Sea-salt	H_2SO_4-acid
Composition mode-1	15	10	60	0	15
Composition mode-2	20	50	15	0	15
Composition mode-3	10	10	5	60	15
Aerosol density	1.85	1.85	2.0	2.45	1.835
Type of activity	Continental	—	—	Maritime	H_2SO_4
Solubility	Soluble	Insoluble	Insoluble	Soluble	Soluble
Refractive index $m_{0.45}$	1.53–0.005*i*	1.53–0.008*i*	1.75–0.454*i*	1.50–0.000*i*	1.40–0.000*i*
Refractive index $m_{0.55}$	1.53–0.006*i*	1.53–0.008*i*	1.75–0.440*i*	1.50–0.000*i*	1.37–0.000*i*
Refractive index $m_{0.63}$	1.53–0.006*i*	1.53–0.008*i*	1.75–0.430*i*	1.49–0.000*i*	1.37–0.000*i*

(b)

R.h.	$r_{eff,w}$	V_w	λ	β_{ext}	$\tilde{\omega}$	g
			0.45	0.048628	0.84874	0.6607
00%	0.211	6.882	0.55	0.037370	0.82368	0.6230
			0.63	0.030454	0.80384	0.5927
			0.45	0.062292	0.86905	0.6827
50%	0.241	9.737	0.55	0.048444	0.85026	0.6481
			0.63	0.039793	0.83517	0.6193
			0.45	0.109188	0.91377	0.7306
90%	0.407	26.11	0.55	0.085507	0.90391	0.7111
			0.63	0.071923	0.89703	0.6892

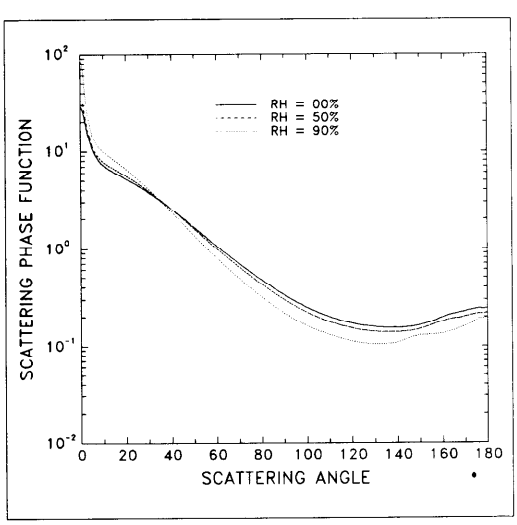

Fig. 5. Relative humidity dependence of scattering phase functions of aerosols, defined as in Table 3, for (a) —— 0%, (b) – – – 50%, and (c) · · · 90%.

forward peak when relative humidity is increased. This nonlinearity can be seen from the values listed in Table 3b in which the effective radius is doubled for an increase in relative humidity from 50 to 90% while only a 10% increase in particle size occurs for moisture changes from dry to 50% relative humidity.

Since the model atmosphere adopted in this study consists of Rayleigh scattering, gaseous absorption and aerosol particle extinction, it is necessary to determine an effective optical depth, single scatter albedo and scattering phase matrix for the combined effects. These quantities can be written as

$$\tau_{eff}=\tau_R+\tau_G+\tau_H$$
$$\tilde{\omega}_{eff}=(\tau_R+\tilde{\omega}_H\tau_H)/\tau_{eff}$$
$$P_{eff}=(\tau_R P_R+\tilde{\omega}_H\tau_H P_H)/\tilde{\omega}_{eff}\tau_{eff}, \qquad (6)$$

where R, G and H refer to Rayleigh, gas and haze, respectively.

4. RADIATIVE TRANSFER MODEL

4.1. *Basic equation and solution*

We begin with the monochromatic one-dimensional equation which is simply an energy conservation law for radiative transfer through the optical medium. In this model, aerosol particles are assumed to lie in a horizontally homogeneous atmosphere (i.e. plane-parallel). As such, the intensity field (I) varies spatially only in the vertical direction (z or τ), and has a zenith (θ) and azimuth (ϕ) angle dependence.

The transfer of monochromatic radiation through an infinitesimally thin layer can be expressed as (Chandrasekhar, 1960)

$$\mu\frac{dI(z;\mu,\phi)}{\beta_{ext}dz}=-I(z;\mu,\phi)+J(z;\mu,\phi), \qquad (7)$$

where $\mu=\cos\theta$. The first term on the right side of Equation (7) represents the loss of intensity by extinction through the layer and the second term is the contribution to the intensity field through the effects of sources within the layer. For visible radiation, the source function (J) is given as

$$J(\tau;\,\mu,\phi)=\frac{\tilde{\omega}}{4\pi}F_0P(\tau;\,\mu,\phi,\,-\mu_0,\,\phi_0)e^{-\tau/\mu_0}$$
$$+\frac{\tilde{\omega}}{4\pi}\int_0^{2\pi}\int_{-1}^{1}P(r;\mu,\phi,\mu',\phi')I(\tau;\,\mu',\phi')d\mu'd\phi', \quad (8)$$

where F_0 is the monochromatic flux at the top of the atmosphere. The optical depth (τ) is a product of the volume extinction coefficient (β_{ext}) and the geometrical thickness of the layer. τ is conventionally set to zero at the top of the atmosphere and increases, in a positive sense, toward the surface. The single-scatter albedo ($\tilde{\omega}$) and scattering phase matrix ($P(\tau;\,\mu,\phi,\mu',\phi')$) are defined previously. This source function is composed of the contribution from the single scatter of the collimated solar flux at top (first term of Equation (8)) and the contribution from multiple scattering processes within the layer (second term). The geometry of the model is depicted schematically in Fig. 6.

The internal and emergent diffuse intensities of the haze layer and the atmosphere are determined by solving Equation (7). A variety of methods exist for this purpose (cf. Lenoble, 1985 for a detailed review). A typical technique involves expanding the phase matrix and intensity about the azimuth as follows:

$$P(\tau;\,\mu,\phi,\mu',\phi')=\sum_{m=0}^{N-1}P^m(\tau;\,\mu,\mu')\cos m(\phi-\phi')$$
$$I(\tau;\,\mu,\phi)=\sum_{m=0}^{N-1}I^m(\tau;\,\mu)\cos\,m(\phi-\phi'_0). \quad (9)$$

A set of N differential equations is obtained which is systematically solved for the N unknown amplitudes I^m by utilizing the methods of Doubling and Adding (van de Hulst, 1963; Grant and Hunt, 1969). Therefore, the solution is obtained by applying the boundary conditions at the top of the atmosphere and the surface, respectively, as follows:

$$I_0(\tau=0;\,-\mu,\phi)=\frac{F_0}{4\pi}\delta(\mu-\mu_0)\delta(\phi-\phi_0)$$
$$I(\tau=\tau^*;\,\mu,\phi)=A_sI(\tau=\tau^*;\,-\mu',\phi'), \quad (10)$$

where δ is the Dirac delta function, τ^* is the optical depth at the surface and A_s is the albedo of the surface. The first condition implies that there is no diffuse intensity entering the top of the atmosphere, except for the collimated solar beam. The second condition defines the reflection of the diffuse intensity at the surface. For simplicity, the reflecting surface is assumed to be Lambertian.

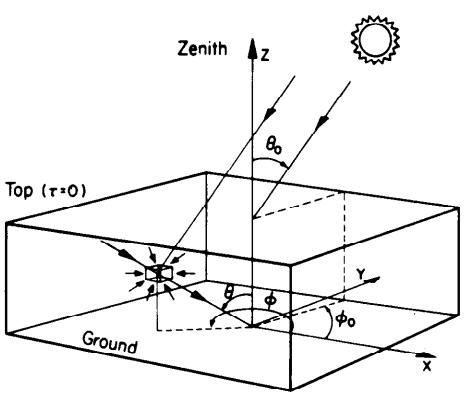

Fig. 6. Schematic representation of geometry for a plane–parallel atmosphere. Inhomogeneity of optical properties is considered only in the vertical direction.

4.2. *Visibility and contrast*

The apparent spectral intensity (or radiance, Equation (7)) of an object seen from a distance in an atmosphere is a result of the contributions from the background intensity and the residual intensity of the object. The background intensity along a hypothetically infinite path defines the equilibrium intensity I_q (Duntley *et al.*, 1957). In a plane–parallel atmosphere, the optical properties are uniform along horizontal paths; thus, I_q can be written as

$$I_q(\tau^*;\,\phi)=\frac{\tilde{\omega}}{4\pi}F_0P(\tau^*;\,\mu=0,\,\phi,\,-\mu_0,\phi_0)e^{-\tau^*/\mu_0}$$
$$+\frac{\tilde{\omega}}{4\pi}\int_0^{2\pi}\int_{-1}^{1}P(\tau^*;\,\mu=0,\phi,\mu',\phi')$$
$$\times I(\tau^*;\,\mu',\phi')d\mu'd\phi', \quad (11)$$

and represents the contribution from the sky through both single and multiple scattering (path radiance of Equation (8)). Therefore, the apparent intensity of an object is described by the simple expression (we omit the angular dependence)

$$I_t=I_0T_r(0,r)+I_q(1-T_r(0,r)), \quad (12)$$

where r refers to the distance between the object and the observer and T_r is the transmittance of the object image forming intensity (I_0) along the path.

An important factor when viewing an object at the horizon is how clearly it can be seen against the background sky. One way to quantify the visibility is in terms of the equilibrium contrast (C_q) which is given as (Duntley *et al.*, 1957)

$$C_q=\frac{(I_0-I_q)\,Tr(0,r)}{I_q}. \quad (13)$$

The object image forming intensity is expressed as

$$I_0=\frac{1}{4\pi}A_0F_0e^{-\tau^*/\mu_0}, \quad (14)$$

where A_o is the albedo of the object. For the case of viewing a black object in a vacuum, $C_q = -1$. When $C_q = 0$, there is no contrast with the background and the object can not be seen and $C_q > 0$ for optically lighter objects.

4.3. *Colorimetric parameters and color contrast*

Another way to assess visual air quality is in terms of color contrast. An observer's actual perception of the color of a light beam can only be characterized in a qualitative manner. The psychological description of an observer's visual sensation often includes brightness, hue and saturation. These psychological terms loosely correspond to the following psychophysical terms: luminance, dominant wavelength and spectral purity (colorimetric parameters). To clarify these colorimetric parameters the chromaticity diagram is reproduced and modified from the treatise of "The Science of Color" (Optical Society of America, 1953) and "Color Measurement" (Grum and Bartleson, 1980), as shown in Fig. 7. A plane of constant luminance is represented as the shaded triangular area and the strength of luminance decreases along the $\mathscr{Z}$ axis toward the point $\mathscr{O}$. The horseshoe shaped region consists of all real colors and the boundary of this region represents pure monochromatic color (or dominant wavelength). Points that lie within the confines of the diagram are considered to be less saturated than the pure colors. Pure white light is represented by an equal proportion of three primaries: red, green and blue light. The ratio of the distance between a sample color and the white light to the distance of its dominant wavelength and the white light is defined as spectral purity.

The work of Dave (1980, 1981) includes perhaps the most sophisticated description of sky colors; however, they were shown in some sort of three-dimensional plots of the colorimetric parameters. It is evident that the actual sky color must be interpreted rather subjectively from the plots of the colorimetric parameters. Thus, it is desirable to create sky color maps to assess changes in sky color.

To recreate the stimuli that produce the color sensation, an additive mixture of lights (e.g. Optronics Optical Film Writer) or a subtractive mixture of pigments (such as cyan, magenta and yellow used in the HP-PaintJet color printer) has been chosen to match the color perceived by the observer. The former color-

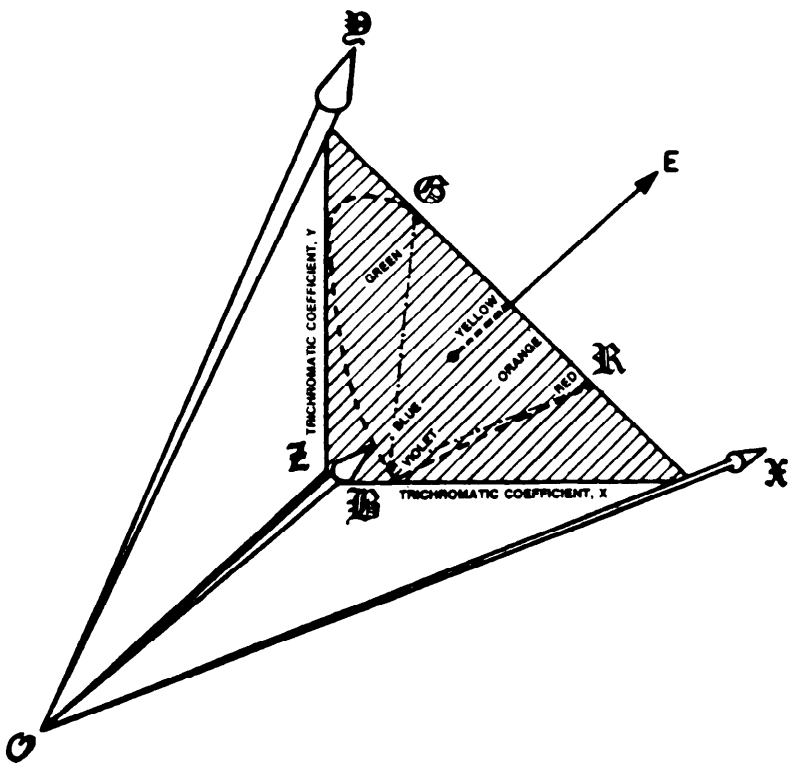

Unit plane of equal luminance showing intersection points of the CIE imaginary primaries $\mathfrak{X}, \mathfrak{Y}, \mathfrak{Z}$, and real spectral primaries $\mathfrak{R}, \mathfrak{G}, \mathfrak{B}$.

Fig. 7. CIE chromaticity diagram (see text), modified from Grum and Bartleson (1980).

matching method is referred to as the tristimulus specification of color, in which the proportions of three primary lights (red $\mathscr{R}$, green $\mathscr{G}$ and blue $\mathscr{B}$ of Fig. 7) are determined and the chromaticity diagram is subsequently used to specify the color. However, a chromaticity match cannot be fully made for all real stimuli or for all aspects of visual color perceived by an observer. For example, an urban brown haze may be interpreted as some shade of gray by the chromaticity calculations (Malm *et al.*, 1980). Therefore, it is better to quantify color in a relative sense such as a color contrast. A state-of-the-art Optronics optical Film Writer, which generates a 900×1350 pixel resolution on 35 mm slides, is used in this study.

The Optronics Film Writer is essentially a sophisticated camera, which is digitally-controlled to plot optical densities on photographic film. The monochromatic optical density of an ith pixel (D_i) is obtained simply as a logarithmic transformation of the transmittance ($\mathscr{T}$) of the film

$$D_i = \log_{10} \frac{1}{\mathscr{T}_i}, \tag{15}$$

where $\mathscr{T}_i$ is defined as a ratio of the transmitted radiance (I_i) to the incident radiance (I_0). Similarly, the optical density of a reference pixel (D_r) also can be obtained, in which the strongest transmitted intensity in the radiance field is chosen as the reference or contrast,

$$D_i - D_r = \log_{10} \frac{1}{\mathscr{T}_i} - \log_{10} \frac{1}{\mathscr{T}_r} \quad \text{or}$$

$$D_i = D_r - \log_{10} \frac{I_i}{I_r}. \tag{16}$$

Then, the optical density is related to the Film Writer intensity (digital number) through the gray scale calibration curves, as shown in Fig. 8 for 25 μm grid. The intensity of light source varies in 256 steps (0 for white and 255 for black). Theoretically, the Film Writer should be able to produce about 16.7 million colors ($256 \times 256 \times 256$). However, due to the limited range of film sensitivity and of perceived color change by an average observer, colors that can be identified are far less than this number. Color images can be rendered by exposing the film sequentially through the three primary lights, and correcting for the interactions between the cyan, magenta, and yellow film dyes (Johnson *et al.*, 1988).

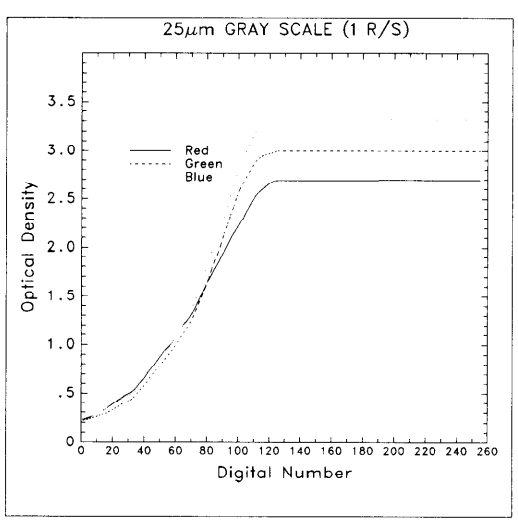

Fig. 8. 25 μm gray scale curves between optical density and digital number used in the Optronics Film Writer for three primary lights.

5. MODEL RESULTS

The following results from both Mie model and radiative transfer model computations are carried out on a personal computer and a VAX-2000 workstation. A simple two-layer atmosphere is used and the top of the upper layer is set at 30 km height, overlying a 2 km thick boundary layer. Monochromatic flux incident at top of the atmosphere is normalized to unity and the wavelengths of the three primaries are chosen as 0.63 μm for red, 0.55 μm for green and 0.45 μm for blue.

5.1. *Sensitivity studies on sky radiance*

The most difficult aspect of solving the equation of radiative transfer is the numerical evaluation of the integral in the multiple scattering term. A finite sum of Legendre polynomials is used to approximate the phase matrix, in which the determination of the number of necessary terms is typically a trade-off between accuracy and computational speed. King (1983) demonstrated the dependence of the number of terms on the phase matrix used. To obtain a criterion for computational efficiency, Figs 9a and 9b show the sensitivity of sky radiance to the number of discrete streams (2 times the hemispheric quadratures). The sun illuminates from above along a 60° zenith sngle and the sky radiances are computed at a zenith angle of 60° with various azimuthal angles. The scattering phase functions of sea-salt and all components (Fig. 3) are used. Sky radiances converge very fast for azimuthal angles other than the forward direction. Since the sea-salt component has a strong forward peak in scattering phase matrix, more terms are needed to resolve this feature. Therefore, 16 quadrature points for hemispheric discretization are the least requirement for this study.

The sensitivity of sky radiance on the aerosol species, as well as on the incident solar zenith angle and surface reflectance, is examined using sky maps in Figs 10a f. The optical properties used in the sky radiance computations are identical with those in Table 2 and Fig. 3, except that the total optical depth of each aerosol component is specified to be 0.1 which is

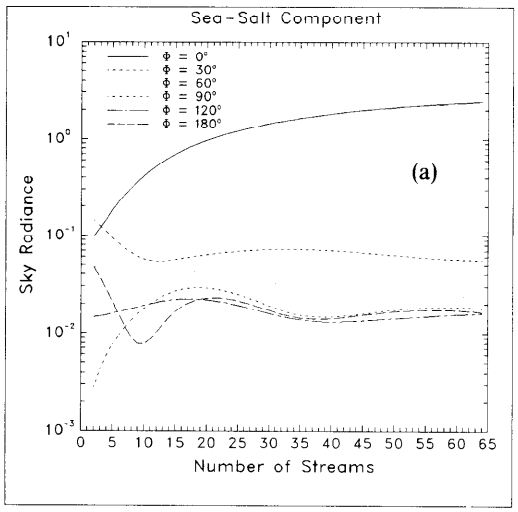

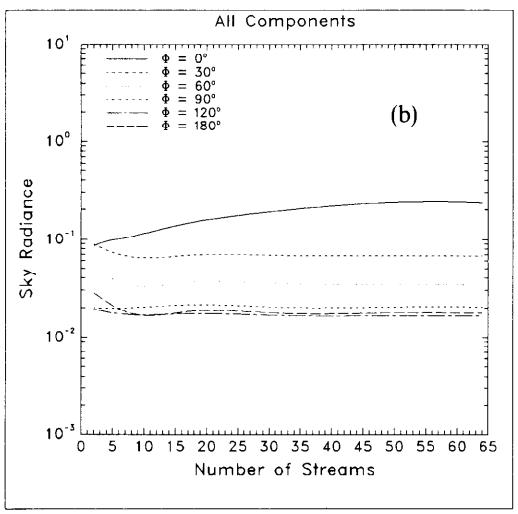

Fig. 9. Sensitivity studies of diffuse sky radiance on number of discrete quadratures used in the radiation model: (a) sea-salt component and (b) all components for various azimuth angles.

typical of atmosphere turbidity values. Figures 10a–10d, respectively, correspond to cases of soot, dust-like, sea-salt, and all components concerned under the conditions of a black surface and 60° solar illumination at the top. What is characteristic of these atmospheres is the well-known limb brightening near the horizon. Sky brightness increases, in general, with increasing atmospheric turbidity and/or path length due to the more diffuse character of the radiance field. The phase functions of soot and dust-like aerosols are generally smooth, which produce nearly circular concentric contours. Since soot is more absorptive than dust-like aerosols, the sky radiance field by soot is about half the strength of that by dust-like aerosols. Sea-salt aerosols, by contrast, are large and nearly pure scatterers and for this case, shown in Fig. 10c, the intensity increases substantially near the sun. This is due, primarily, to the strong forward scattering from the sea-salt aerosols. This aureole region around the solar point is also retained but is weaker when the composite aerosol model is used, as shown in Fig. 10d. The maximum intensity occurs at the sun-side horizon of the principle plane as a result of multiple scattering.

With the inclusion of a Lambertian surface with a reflection of 0.15 below an atmosphere containing the composite aerosol model, the horizon light (Figs 10d vs 10e) is enhanced especially for low solar elevation. As the sun is moved towards zenith, the maximum diffuse radiance shifts to the solar point and sky radiances become circular concentric when the sun is right over the zenith.

5.2. *Equilibrium intensity and contrast*

The following results of equilibrium intensity (I_q) and contrast (C_q) were computed assuming a dark object ($A_o = 0.25$) and a path length (object–observer distance) of 20 km. Figures 11a and 11b show the azimuthal dependence of equilibrium intensity and contrast, respectively, for an aerosol model defined in Table 2. The solar zenith angle is 60° and the computations were made assuming no surface reflection (thin curves) and a surface reflectivity of 0.15 (thick curves). It is evident from Fig. 11a that I_q takes on the behavior of the scattering phase function (Fig. 3). This indicates that the background sky radiance viewed along a horizontal path is highly dependent on the aerosol phase function. As expected, I_q increases systematically due to the additional intensity along the line of sight that arises from reflection by the underlying surface. Since forward scattering is more pronounced for anisotropic aerosol scattering, the relative increase in I_q due to surface reflection is the largest at the sun side.

Figure 11b shows C_q as a function of ϕ for the same aerosol model used in Fig. 11a. C_q is inversely proportional to I_q under the assumption of horizontal homogeneity (Equation (13)). We have employed an identical optical depth of 0.1 for these cases. Thus the curves of C_q in Fig. 11b have an inverted shape of I_q in Fig. 11a. Since the dark object is contrasted against the brighter background, the largest contrast can be found on the sun side (the largest I_q). But the largest improvement of contrast (ΔC_q), due to the increase of I_q by surface reflection, is found at the anti-sun side (Fig. 11b). This is because ΔC_q is inverse proportion to ΔI_q.

Figures 12a and 12b show the azimuthal variation of equilibrium intensity and contrast for an aerosol model defined in Table 3. Computations were made for a relative humidity of 0%, 50% and 90% with $\theta_o = 60°$ (thin curves) and $\theta_o = 30°$ (thick curves), in which the surface albedo is set to zero. From Table 3b, the corresponding optical depths for a 2 km thick aerosol layer are 0.075, 0.097, 0.17 at 0%, 50%, and

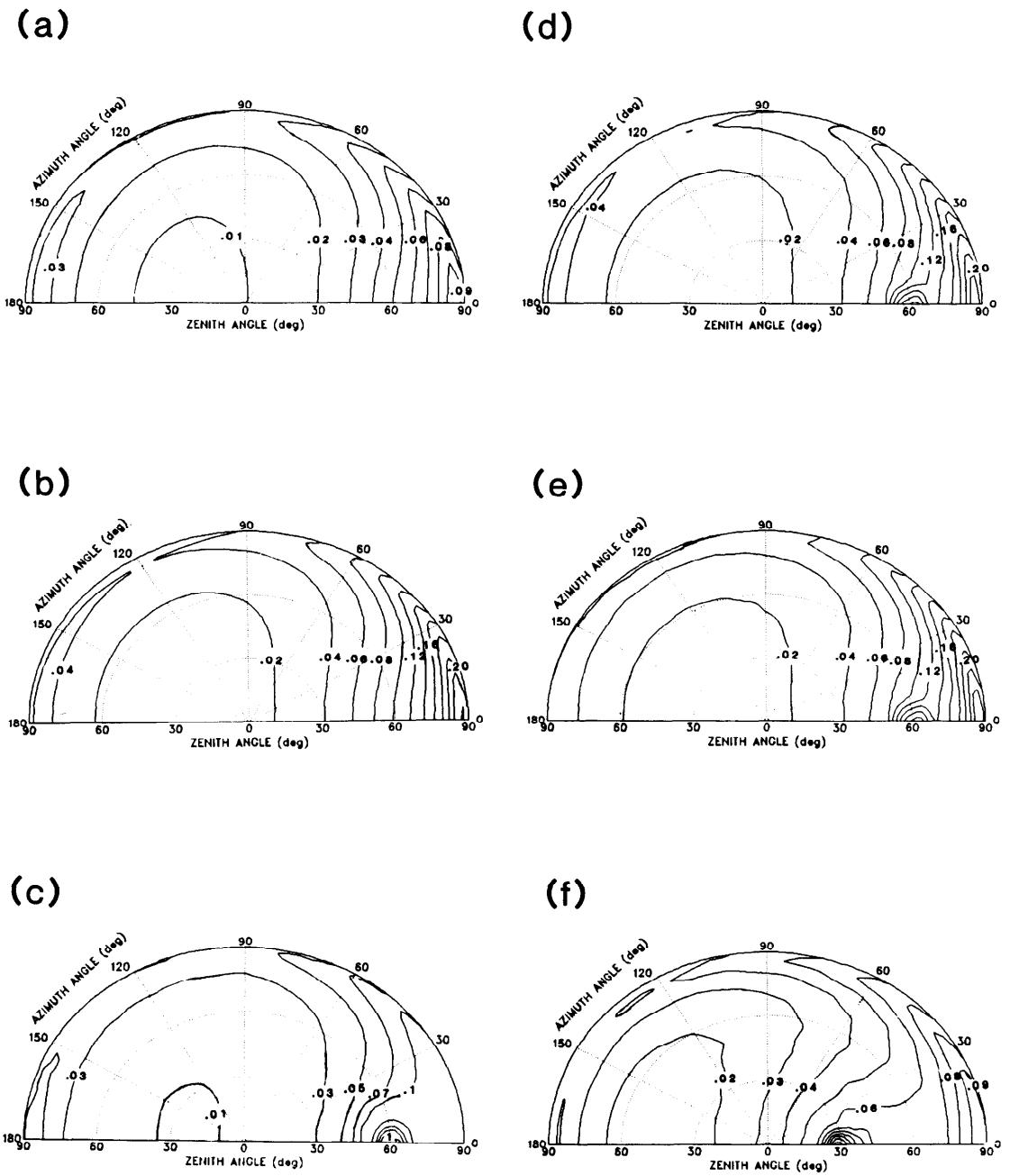

Fig. 10. Zenith–azimuth plot of diffuse sky radiance for various aerosols and boundary conditions: (a) soot, (b) dust-like, (c) sea-salt, and (d) all components. Figures 10a–10d are produced under the boundary conditions of $\theta_o = 60°$ with a Lambertian surface reflection $A_s = 0$ and 10e as in 10d, except $A_s = 0.15$; 10f as in 10d, except $\theta_o = 30°$.

90% relative humidity, respectively. Generally, Fig. 12a shows the same trends as in Fig. 11a. The equilibrium intensity at 90% is very low due to intense scattering in the forward direction, in which case little radiation is scattered toward the horizon. As the sun moves toward zenith, I_q decreases further (cf. Fig. 10). Similarly, the discussion in Fig. 11b generally applies to Fig. 12b but there are differences. For example, at a 90% relative humidity, a dark object is contrasted against either a brighter, indistinguishable, and even darker background depending on the azimuthal direction. Also, the changes in contrast (ΔC_q) for different relative humidities are complicated functions of solar zenith angles, since I_o and T_r (0,2 km) in Equation (13) are no longer a constant for different relative humidity values. The net effect on equilibrium contrast is a result of the competition among the three factors of I_q I_o and T_r. This figure illustrates how equilibrium

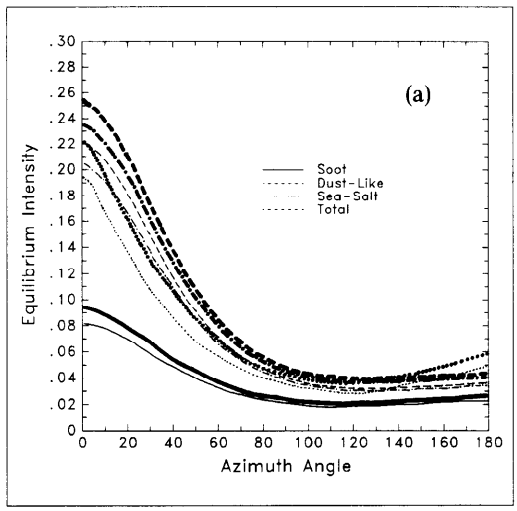

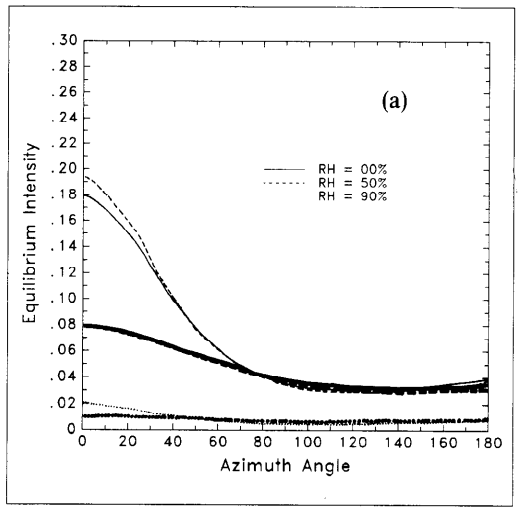

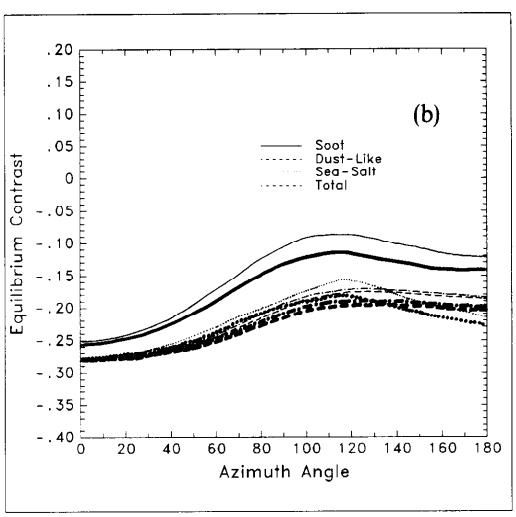

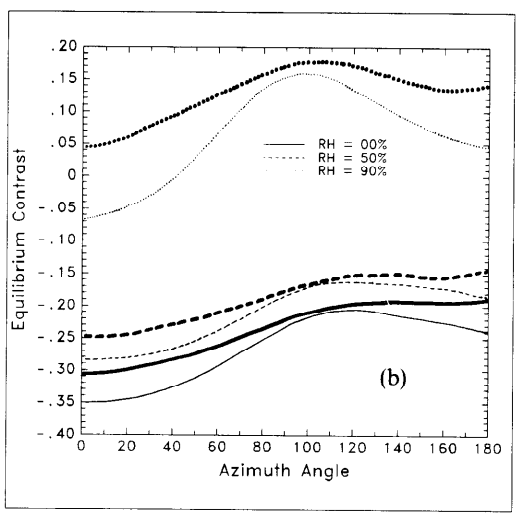

Fig. 11. (a) Equilibrium intensity and (b) equilibrium contrast as a function of azimuth angle for an aerosol model defined in Table 2. Results were computed at 0.55 μm and $\theta = 60°$ with no surface reflection (thin curves) and with a surface reflectivity of 0.15 (thick curves).

Fig. 12. (a) Equilibrium intensity and (b) equilibrium contrast as a function of azimuth angle for an aerosol model defined in Table 3. Results were computed at 0.55 μm and a black surface with $\theta = 60°$ (thin curves) and $\theta = 30°$ (thick curves).

contrast can change dramatically for even an optically thin aerosol layer.

5.3. *Sky color maps*

Four simulated sky color maps obtained directly from the output of the Optronics Film Writer are displayed here. The model conditions are the same as for the previously described results except that the aerosol conditions are varied. Figure 13a shows, for $\theta_o = 30°$ and $\tau_h = 0$, the blue sky which is typical of Rayleigh scattering. What is also characteristic of this atmosphere is the rapid desaturation of the blue color near the horizon. When a more extreme case of a pure scattering aerosol layer (Haze-L) of thickness $\tau_h = 1$ is introduced into the model, as shown in Fig. 13b, the most prominent changes are the lack of blue sky away from the sun and the slight yellowish hue near the sun. The rest of the sky appears a desaturated blue.

For an aerosol model defined in Table 3 at 0% relative humidity and $\theta_o = 30°$, Fig. 13c shows a narrow and dull white aureole around the sun. For the most part, the sky still retains the Rayleigh scatter blue color. When the relative humidity increases to 90%, as shown in Fig. 13d, the most apparent effects are the increased size of the white aureole and the appearance of a dull white color across most of the sky on the sunside. As expected, the sky color for an aerosol atmosphere at 50% relative humidity lies somewhat

between the sky colors corresponding to 0% and 90% relative humidity. When a surface reflection of 0.15 is included in the model of Fig. 13c, a further desaturation of blue sky at the horizon is found as predicted in the previous section. A similar feature is also seen when the sun moves toward the horizon.

6. SUMMARY

The objectives of this paper are to study the effects of various microstructures of atmospheric aerosols on their optical properties and the subsequent influence of these properties on the computation of path radiance and contrast. Mie computations are performed, in which the physical properties of aerosols and the relative humidity of model atmosphere are allowed to vary. A plane–parallel multiple scatter radiation model was used to demonstrate how aerosol particles impact on visibility and visual air quality. Solutions to the radiative transfer equation were obtained using the methods of doubling and adding. The results in this paper were obtained using a simple two layer model and at least a 16-quadrature (i.e. 32-stream) discretization.

It has been shown that a thin aerosol layer can influence visibility by increasing the diffuse sky intensity, which in turn changes the contrast of an object viewed along a horizontal path. The sensitivity of the sky radiance to aerosol species as well as incident solar zenith angle and surface reflectance is examined. It is found that for horizontal paths the equilibrium intensity takes on the behavior of the scattering phase function. This in turn indicates that the background sky radiance viewed along a horizontal path is highly dependent on the structure of aerosol phase function. The effects of surface reflection and solar zenith angle on the equilibrium contrast lead to a dynamical change in contrast, depending on how and what object is viewed and most important what aerosol microstructure defines the optical properties of the aerosol.

In addition, color maps were used to assess the impact of aerosols on sky color. These maps were created by the Optronics Film Writer. It was shown that a thin aerosol layer produced a distinct white aureole around the sun. The most dramatic changes in sky color occurred when the aerosol optical thickness increased and also when relative humidity increased. In those cases much of the sky on the sun side exhibited a dull white color and the aureole assumed a light yellowish appearance.

Acknowledgements—The authors are grateful to Dr William C. Malm for his discussion in color contrast and to Lawrence Mauch, James R. Hein and John V. Molenar of the National Park Service, for providing us the assistance of the Optronics Film Writer system. This research was supported by the National Park Service through the Cooperative Institute for Research in the Atmosphere (CIRA), Grant NA 81RA-H-001.

REFERENCES

Ackerman T. P. and Toon O. B. (1981) Absorption of visible radiation in atmosphere containing mixtures of absorbing and nonabsorbing particles. *Appl. Opt.* **20,** 3661–3667.

Aitchison J. and Brown J. A. C. (1957) *The Log-normal Distribution.* Cambridge University Press, Cambridge.

Barone J. B., Cahill T. A., Eldred R. A., Flocchini R. G., Shadoan D. J. and Dietz T. M. (1978) A multivate statistical analysis of visibility degradation at four California cities. *Atmospheric Environment* **12,** 2213–2221.

Bigg E. K. (1980) Comparison of aerosol at four baseline atmospheric monitoring stations. *J. appl. Met.* **19,** 521–533.

Blanchet J. and List R. (1983) Estimation of optical properties of arctic haze using a numerical model. *Atmospheric–Ocean* **21,** 444–465.

Bohren C. F. (1986) Applicability of effective-medium theories to problems of scattering and absorption by nonhomogeneous atmospheric particles. *J. atmos. Sci.* **43,** 468–475.

Chandrasekhar S. (1960) *Radiative Transfer.* Dover, New York.

Chýlek P., Grams G. W. and Pinnick R. G. (1976) Light-scattering by irregularly randomly oriented particles. *Science* **193,** 480–482.

Dave J. V. (1980) Simulation colorimetry in the earth–atmosphere system. *Rem. Sens. Envir.* **9,** 301–324.

Dave J. V. (1981) Transfer of visible radiation in the atmosphere. *Atmospheric Environment* **15,** 1805–1820.

Davies C. N. (1974) Size distribution of atmospheric particles. *J. Aerosol Sci.* **5,** 293–300.

Deirmendjian D. (1969) *Electromagnetic Scattering on Spherical Polydispersions.* Elsevier, New York.

Duntley D., Boileau A. and Preisendorfer R. (1957) Image transmission by the troposphere. *J. Opt. Soc. Amer.* **47,** 499–506.

Egan W. G. (1982) Volumetric scattering and absorption by aerosols: parametric sensitivity in Mie modeling and comparisons to observations. *Appl. Opt.* **21,** 1445–1453.

Friedlander S. K. (1970) The characterization of aerosols distributed with respect to size and chemical composition. *J. Aerosol Sci.* **1,** 295–307.

Grant I. P. and Hunt G. E. (1969) Discrete space theory of radiative transfer I. Fundamentals. *Proc. Roy. Soc. Lond.* **A. 313,** 183–197.

Groblicki P. J., Wolff G. T. and Countess R. S. (1981) Relationships between extinction and chemical composition for the visibility-reducing species in the Denver "brown cloud". *Atmospheric Environment* **15,** 2473–2484.

Grum F. and Bartleson C. J. (1980) *Optical Radiation Measurements. Vol.* 2: *Color Measurement.* Academic Press, New York.

Hänel G. (1976) The properties of atmospheric aerosol particles as functions of the relative humidity at thermodynamic equilibrium with the surrounding moist air. *Adv. Geophys.* **19,** 73–188.

Hansen J. E. and Travis J. B. (1974) Light scattering in planetary atmospheres. *Space Sci. Rev.* **16,** 527–610.

Holland A. C. and Gagne G. (1970) The scattering of polarized light by polydisperse systems of irregular particles. *Appl. Opt.* **9,** 1113–1121.

Johnson C. E., Malm W. C., Molenar J. V., Mauch L. and Hein J. R. (1991) Improved methods for the computer-imaging of haze layers. *APCA J.* (in press).

Kerker M. (1969) *The Scattering of Light and Other Electromagnetic Radiation.* Academic Press, New York.

King M. D. (1983) Number of terms required in the Fourier expansion of the reflection function for optically thick atmospheres. *J. Quant. Spectrosc. Radiat. Transfer* **30,** 143–161.

Lenoble J. (1985) *Radiative Transfer in Scattering and Absorbing Atmospheres: Standard Computational Procedures.* A. Deepak, Hampton, VA.

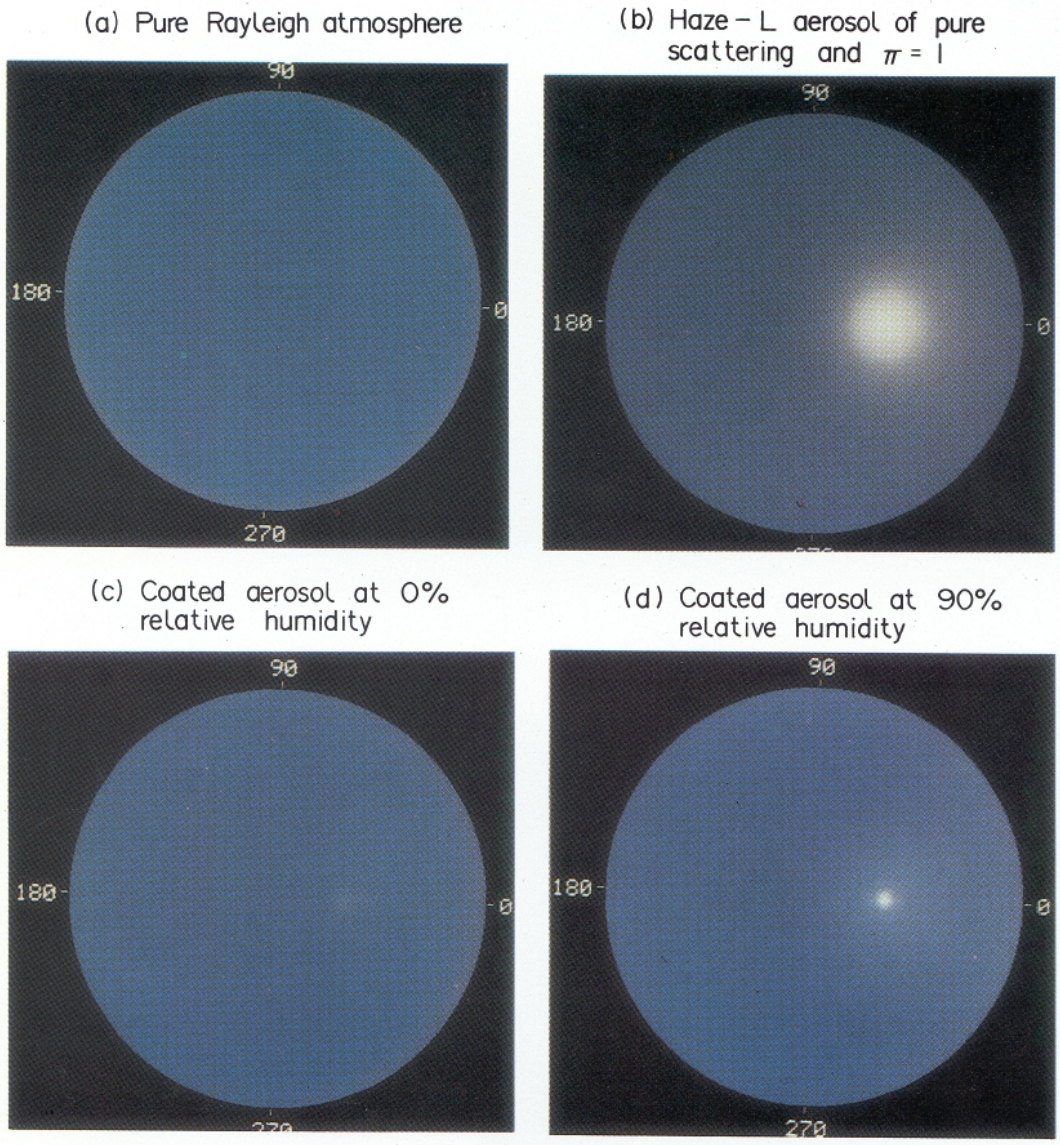

Fig. 13. Simulated sky color maps for (a) pure Rayleigh atmosphere, (b) aerosol Haze-L model of pure scattering and $\tau = 1$, (c) aerosol model defined in Table 3 at 0% relative humidity, and (d) as in (c), but for 90% relative humidity. Results are shown at $\theta = 60°$ with no surface reflection. Numbers surrounding image represent the azimuth angles; the zenith angle is defined as 0° at the center of image and 90° at the perimeter.

Malm W. C., Leiker K. K. and Molenar J. V. (1980) Human perception of visual air quality. *APCA J.* **30,** 122–131.

Megaw W. J. (1977) Thin layer brown haze. *J. Aerosol Sci.* **8,** 21–29.

Nair P. V. N. and Vohra K. G. (1975) Growth of aqueous sulfuric acid droplets as function of relative humidity. *J. Aerosol Sci.* **6,** 265–271.

Nilsson B. (1979) Meteorological influence on aerosol extinction in the 0.2–40 μm wavelength range. *Appl. Opt.* **18,** 3457–3473.

Optical Society of America (1953) *The Science of Color.* Thomas Y. Crowell, New York.

Ouimette J. R. and Flagan R. C. (1982) The extinction coefficient of multicomponent aerosols. *Atmospheric Environment* **16,** 2405–2419.

Pollack J. B. and Cuzzi J. N. (1980) Scattering by nonspherical particles of six comparable to a wavelength: a new semi-empirical theory and its application to tropospheric aerosols. *J. atmos. Sci.* **37,** 868–881.

Shettle E. P. and Fenn R. W. (1979) Models for the aerosols of the lower atmosphere and the effects of humidity variations on their optical properties, report no. AFGL-TR-0214, Hanscom AFB, MA.

Sloane C. S. (1984) Optical properties of aerosols of mixed composition. *Atmospheric Environment* **18,** 871–878.

Sloane C. S. (1986) Effect of composition on aerosol light scattering efficiencies. *Atmospheric Environment* **20,** 1025–1037.

Toon O. B. and Ackerman T. P. (1981) Algorithms for the calculation of scattering by stratified spheres. *Appl. Opt.* **20,** 3657–3660.

van de Hulst H. C. (1963) *A New Look at Multiple Scattering.* Goddard Institute for Space Studies, NASA, New York.

Wiscombe W. J. (1980) Improved Mie scattering algorithms. *Appl. Opt.* **24,** 1505–1509.

Wiscombe W. J. (1991) Further improvements in Mie scattering algorithms. *Appl. Opt.* (in press).